AIAA JOURNAL
Vol. 44, No. 10, October 2006

Hypervelocity Fuel/Air Mixing in Mixed-Compression Inlets of Shcramjets

Derrick C. Alexander* and Jean P. Sislian†
University of Toronto Institute for Aerospace Studies, Toronto, Ontario M3H 5T6, Canada
and
Bernard Parent‡
Nagaoka University of Technology, Nagaoka 940-2188, Japan

DOI: 10.2514/1.12630

This paper investigates the mixing of hydrogen fuel with air in the mixing duct of a mixed-compression shock-induced combustion ramjet (shcramjet) inlet. Mixing augmentation through the use of cantilevered ramp injector arrays on opposite shcramjet inlet walls is studied and the influence of relative array locations is quantified. Studies were undertaken numerically using the WARP code that solves the Favre-averaged Navier–Stokes equations closed by the Wilcox k–ω turbulence model. Air-based mixing efficiencies of up to 0.58–0.68 were achieved with thrust potential losses less than that gained from high-speed fuel injection. Shocks created from the fuel injector structures play a major role in the mixing behavior of the fuel jets on the opposing side of the mixing duct. Chemically reacting studies verified for the correct selection of spanwise displacement of the fuel injectors, an air buffer created between the fuel and walls suppresses premature ignition while still allowing for a mixing efficiency of up to 0.46–0.54.

Nomenclature

a	=	speed of sound
c	=	species mass fraction
d_w	=	distance from wall to first inner node
$\mathcal{F}_{\text{pot}}$	=	thrust potential
$\mathcal{F}_{\text{pot,ref}}$	=	reference thrust potential at engine inlet
k	=	turbulence kinetic energy
M_c	=	convective Mach number, $(q_1 - q_2)/(a_1 + a_2)$
$\dot{m}$	=	mass flow rate
$\dot{m}_{\text{air,engine}}$	=	mass flow rate of air in engine
p	=	pressure
$p^\star$	=	effective pressure, $p + 2/3\rho k$
Pr_t	=	turbulent Prandtl number
q	=	magnitude of velocity vector
r	=	grid size factor
Sc_t	=	turbulent Schmidt number
T	=	temperature
x_1, x_2, x_3	=	Cartesian coordinates
y^+	=	nondimensional wall distance, $d_w\sqrt{\rho\tau_w}/\mu$
η_m	=	mixing efficiency
μ	=	viscosity
ρ	=	density
τ_w	=	wall shear stress
ϕ	=	equivalence ratio
ω	=	dissipation rate per unit of turbulent kinetic energy

Subscripts

b	=	station of interest
c	=	station of interest reversibly expanded to constant pressure at shcramjet exit area

Superscripts

R	=	reacting
S	=	stoichiometric

Introduction

HYPERSONIC air-breathing engines such as scramjets and shock-induced combustion ramjets (shcramjets) provide a more efficient high-speed vehicle propulsion system than rocket engines. By maintaining supersonic flow throughout such engines, excessive losses that result from decelerating the flow to subsonic velocities, as in ramjets, are avoided. In an external-compression shcramjet, Fig. 1a, oncoming air is compressed by shocks and mixed with fuel injected near the leading edge of the inlet. Combustion is initiated by a shock wave, originating from the cowl or from aerodynamic wedges located just after the start of the cowl. The combustion products are then expanded through a divergent nozzle to provide thrust. In the mixed-compression shcramjet considered in the present paper, Fig. 1b, the fuel is injected, mixed, and compressed with the air in the internal duct of the inlet before the combustion-inducing shock. Studies by Dudebout et al. [1] have shown through two-dimensional solutions of the Euler equations that mixed-compression shcramjets outperform external-compression shcramjets by over 20% in fuel specific impulse for flight Mach numbers between 10 and 23. These studies assumed an optimistic perfectly stoichiometric mixture before the detonation wave. Sislian et al. [2] further examined the effects of off-design flight and incomplete fuel/air mixing on shcramjet performance. Assuming Gaussian distributions of fuel, with peak values along the walls from which fuel is presumed to be injected, it was found that engines designed to produce detonation waves resulted instead in shock-induced/detonation combustion combinations. Incomplete fuel mixing greatly increased ignition delays requiring longer combustor sections for complete combustion. Incomplete mixing in a mixed-compression shcramjet resulted in a 33% drop in specific impulse. This was still superior performance compared with external-compression shcramjets with incomplete mixing up to the highest tested Mach number of 22. None of the previous studies included the actual fuel/air mixing process in the inlet of the engine.

There has been a recent interest in premixing of fuel and air before scramjet combustors in an effort to improve the mixing and burning performance of scramjet engines [3–6]. Sislian and Parent [7], solving the nonreacting Favre-averaged Navier–Stokes equations

Received 2 September 2004; revision received 21 October 2005; accepted for publication 7 May 2006.

*Graduate Student, 4925 Dufferin Street; derrick@caius.utias.utoronto.ca. Student Member AIAA.
†Professor; sislian@caius.utias.utoronto.ca. Associate Fellow AIAA.
‡JSPS Researcher, 1603-1 Kamitomioka; bernard.parent@utoronto.ca.

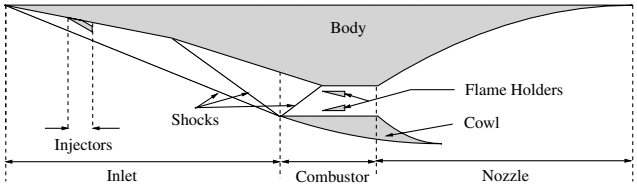

a) External-Compression

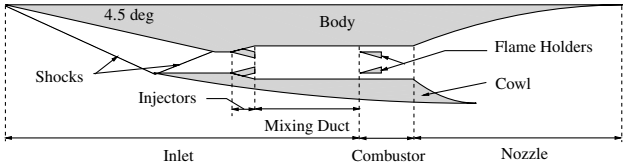

b) Mixed-Compression

Fig. 1 Shcramjet engine schematics.

with the Wilcox [8] k–ω turbulence model, numerically investigated the mixing produced by an optimized cantilevered ramp injector array [9–12] in the inlet of an external-compression shcramjet. The study sought to modify the inlet and injector geometry to improve overall performance in terms of mixing efficiency and losses. Fuel injection was found to account for between a 40 and 120% increase in thrust potential over the losses experienced. By using an injector array in which the injectors alternated between compression angles of 9 and 16 deg, instead of a constant 10 deg compression angle on all the injectors, the maximum mixing efficiency was found to be 0.47. This was a 32% increase over the constant 10 deg array value and was attributed to the separation of the alternate jets and the resulting increased mass of airflow between the jets.

A consequence of the fuel injection in the external-compression inlet was that if the cowl was adjusted for the on-design configuration to lie at the intersection of the inlet shocks, as illustrated in Fig. 1a, then the height of the inlet and mass flow rate entering the inlet were found to be dependent on the mixing process itself. Even in the best mixing case, the limited fuel penetration dictated fuel was found by the end of the inlet to inhabit only 48% of the inlet height. This results from fuel injection on one side of the airstream and the continued compression that forces the fuel towards the body wall.

One of the difficulties in shcramjet fuel/air mixing in the inlet of the engine is the risk of premature ignition of the combustible mixture before the combustion-inducing shock. Premature ignition is found to occur as the combustible mixture enters the hot hypersonic boundary layers. Schwartzentruber et al. [13] included a non-equilibrium chemical model based on that of Jackimoski [14] and showed that suppression of premature ignition in the boundary layer of an external-compression shcramjet is possible with either N_2 or H_2 injection via a backward-facing step to cool the boundary layer downstream of the injector array. Addition of 18% of the total H_2 in the backward step was sufficient to prevent ignition and left the mixing characteristics essentially unaltered from the findings of Sislian and Parent [7].

Mixed-compression shcramjets allow for the possibility of fuel injection from both the body and cowl walls, reducing the relative penetration needed for complete mixing. Schumacher [15] performed a preliminary simulation of cantilevered injector arrays placed on opposite walls of a duct at shcramjet engine conditions. The numerical study was performed using a lower-upper symmetric Gauss–Seidel scheme combined with a symmetric shock-capturing total variation diminishing scheme to solve the Navier–Stokes equations. Effects of turbulence and chemical reactions were not considered. Schumacher found that the combination of opposing axial vortices could contribute to increased mixing over a comparable single array.

The present paper examines by numerical simulation the fuel/air mixing processes generated by arrays of cantilevered ramp injectors placed on opposite, upper and lower, walls of a mixed-compression shcramjet inlet duct, Fig. 2. A parametric study is undertaken by varying the spanwise displacement and vertical separation distances of the injectors, to maximize the mixing efficiency and obtain fuel distributions confined to flowfield regions outside the duct wall boundary layers. Although the employed numerical technique has been validated against available experimental data on hypervelocity fuel/air mixing, presented results are subject to the accuracy of the turbulence model used and its ability to accurately capture the turbulent mixing process.

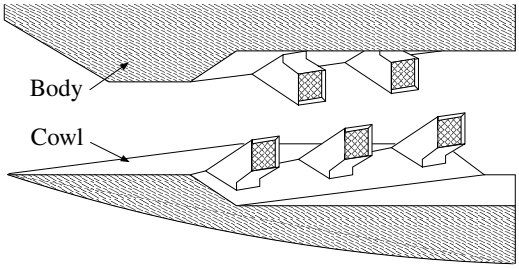

Fig. 2 Injector arrays on opposing duct walls.

Inlet Configuration

The three main factors affecting mixing for injector arrays on opposing walls are the injector geometry, the fuel injection conditions, and the relative injector locations, i.e., the horizontal and vertical distance between the injectors. This study is limited to nonreacting hydrogen/air mixing in an inlet for a flight Mach number of 11 in the U.S. standard atmosphere at an altitude of 34.5 km [16]. The engine inflow conditions are thus a pressure of 601 Pa, temperature of 236 K, and an air velocity of 3391 m/s. The geometry of the mixed-compression shcramjet, as shown in Fig. 1b, is designed such that the shock formed by the leading edge of the body terminates on the cowl lip, and the internal shock formed by the cowl terminates where the inlet turns into the internal duct. The initial 4.5 deg inlet wedge maintains a low temperature in the flowfield to assist in preventing premature ignition in the mixing duct. A horizontal runway in the internal duct, the length of the injector array, is followed by the injector arrays and a 1 m section termed the mixing duct. Subsequent combustor and nozzle flows are not considered in this study.

The configuration of a cantilevered injector arrays is shown in Fig. 3, with the dimensions of the injectors held constant for all cases as shown, unless otherwise specified. The injector arrays are 0.226 m in length and protrude into the airflow with a 5 deg compression angle and expand away from the flow with a 5 deg expansion angle. The fuel injection area is 0.02×0.02 m with a 0.02 m void height under the injector. The array displacement is defined as the distance between the nearest spanwise edges of injectors on opposite walls, and the array separation as the vertical distance between the top surface of the end of the injectors, as illustrated in Fig. 4. Fuel inflow conditions in all cases are specified to provide a global equivalence ratio of one, fuel stagnation temperatures below 1700 K for material

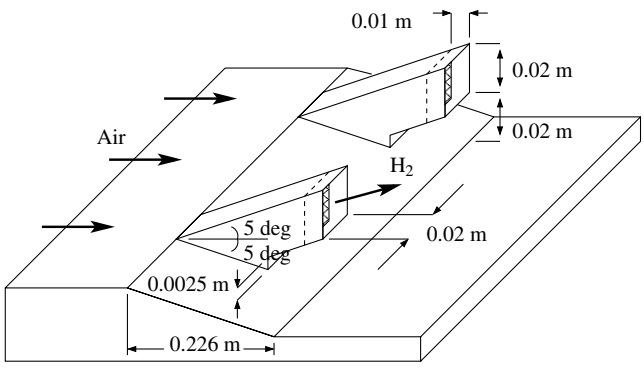

Fig. 3 Cantilevered ramp injector array geometry.

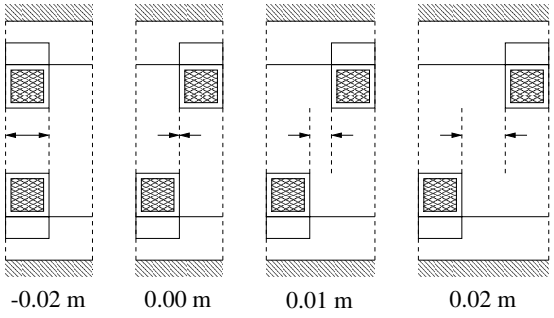

a) Changes in Array Displacement

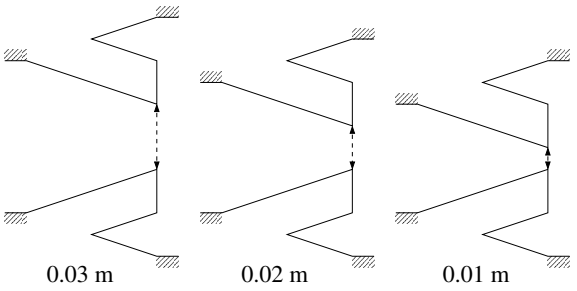

b) Changes in Array Separation

Fig. 4 Opposed injector array geometry changes.

considerations, and static pressures matched to the surrounding airflow. Changes in array locations create a change in the air mass flow through the engine. The inflow velocity of the fuel is modified to meet the aforementioned restraints, creating a variation in convective Mach number, fuel temperature, and fuel density between each case. Typical fuel inflow conditions are thus a Mach number of 4.0, a pressure of 5007 kPa, a temperature of 390 K, and a velocity of 6100 m/s. Table 1 outlines the parametric study of array displacement and separation. Array displacement varies from 0 to 0.02 m and array separation is varied between 0.01 and 0.03 m. In case 1 the array displacement is termed to be −0.02 m where the injectors lie vertically above one another, Fig. 4a, with a spanwise depth of 0.02 m between the computational symmetry planes. In addition to the cases given in Table 1, case 8 is considered for a 0 m array displacement and 0.03 m array separation as in case 2, but only one injector array on the cowl is used with fuel conditions adjusted to maintain a globally stoichiometric mixture. This allows a comparison of the effect of opposed injector arrays to a single array.

Numerical Method

Studies were undertaken numerically using the Window Allocatable Resolver for Propulsion (WARP) code [17,18]. The three-dimensional multispecies Favre-averaged Navier–Stokes equations closed by the Wilcox [8] k–ω turbulence model are solved in generalized curvilinear coordinates to a steady state solution. The Wilcox dilatational dissipation correction is used to account for the effect of reduced shear-layer growth at high convective Mach numbers [19]. This correction has been shown to be necessary when solving similar cantilevered ramp injectors at both matched fuel/air velocities and high convective Mach numbers [18]. A thermally perfect gas is assumed in which entropy, enthalpy, and specific heat at constant pressure are determined via temperature-dependent polynomials from McBride and Reno [20], which are valid over flow temperatures experienced.

The convective derivative is discretized using the Roe scheme in conjunction with Yee flux-limiters [21]. All other terms are discretized via second-order accurate central differencing. The addition of an entropy correction term to the Roe scheme has been shown to detrimentally add diffusion in the shear and boundary layers and is unnecessary for the flows considered herein [10]. Pseudotime iteration is accomplished using implicit Euler time marching, incorporating a block-implicit approximate factorization scheme. The convergence criterion, based on the magnitude of both the continuity and energy residuals, is used to converge the solutions between five and eight orders of magnitude, depending on flowfield location. Convergence is accelerated by the use of the marching window technique that has been shown to decrease work by approximately 10 times and memory by 5 times for similar simulations [17]. This allows for the practical use of finer meshes and higher numerical accuracy. Converged solutions are accomplished in approximately 300 effective iterations for the standard grid density used, with more iterations required for increased grid density.

Table 1 Cases of relative injector location

Array separation, m	Spanwise array displacement, m			
	−0.02	0.00	0.01	0.02
0.01	——	——	Case 7	——
0.02	——	Case 5	Case 6	——
0.03	Case 1	Case 2	Case 3	Case 4

Boundary Conditions

The assumption is made that infinite spanwise arrays are representative of mixing away from the sidewalls of the engine. The initial inlet section before the fuel injectors is therefore solved as a two-dimensional problem. This solution was then implemented across the span 0.038 m before the fuel injectors, with no phenomenon observed to be traveling upstream from the start of the injectors. The three-dimensional domain is 1.26 m long with a typical height and width of 0.11×0.03 m, solved with a typical grid of $317 \times 248 \times 105$ cells.

For the injectors and mixing duct ,second-order symmetry conditions were imposed on the spanwise sides of the computational domain that lie along the centerline of adjacent injectors on opposing walls. All wall surfaces are assumed to be no-slip and fuel-cooled to a constant 800 K. At the walls $k = 0$ and the specific dissipation rate is dependent upon the distance of the first interior node, d_w, as given by Wilcox [8]: $\omega = 36\mu/5\rho d_w^2$.

The start of the inlet was specified as a constant supersonic inflow and the end of the mixing duct as a zeroth-order supersonic outflow. A 10 mm long runway is used inside the fuel injector before the plane of injection to reduce the solution's sensitivity to the freestream value of ω, which is known to cause difficulties in k–ω schemes. The freestream value of k is zero, and the freestream ω is set to 10 times the freestream velocity, which is 100–1000 times smaller then the maximum ω value present at all x_1 planes.

For integration through the laminar sublayer, Wilcox has suggested y^+ should be less than one ([22], p. 371). To maintain practical grid sizes, node spacing at the wall surfaces is 30 μm, resulting in y^+ values between 0.8 and 6.0. Assessment of similar injector cases with a 10 μm wall spacing showed a negligible difference in the boundary layer height or wall shear stress [10].

Grid-Induced Error Assessment

In three dimensions it is impractical to achieve grid refinement great enough to quantify grid-induced error accurately. Only the variation of results between different grid densities is available. Care must be taken because the undulating flow through oblique reflected shocks in a duct can increase numerical dissipation, due to flow not being aligned with the grid lines, from that already produced in the flow by vortical shear layers. Greater grid densities may be needed for the same numerical accuracy as flow aligned with the grid lines. The complex three-dimensional shock patterns in the cases herein dictate that the use of error estimates by means such as Richardson error extrapolation are not valid [23,24]. The overall grid-induced error was evaluated by comparing trends in flowfield properties and performance parameters between grid densities in three dimensions

Table 2 Grid convergence factors

Grid Size Factor, r	1.31	1.15	1.00	0.88	0.77
Nodes (million)	16.9	11.4	7.5	5.1	3.4

to the corresponding variations in the same grid densities for flows in two dimensions.

The results shown in this paper were performed at a grid size factor, r, of 1.0, which corresponds to 7.5 million active nodes ($317 \times 248 \times 105$ grid) for case 3. The grid size factor is proportional to the number of grid lines per meter, so the relative grid-induced error should be similar for the same grid size factor. To evaluate the three-dimensional trends in grid-induced error, case 3 was repeated with a constant ratio of grid size factors as seen in Table 2. Comparisons along lines through the flow show a similar convergence of flowfield properties; see Fig. 5a for the temperature along a line in the x_1 direction at the spanwise center of the domain just below the top of the lower injector ($x_2 = 0.035$ m and $x_3 = 0.015$ m). For the majority of the flow, less than a 3% variation in temperature is found between the coarse and fine meshes, and a less than a 0.8% variation between a grid size factor of 1 and 1.15. The exception is through the strong shock at $x_1 = 0.52$ m where the error between the coarse and fine mesh is 8% and the variation between a grid size factor of 1 and 1.15 is 1.6%. Mass flow averaged quantities agree well, with less than a 1% variation in thrust potential between a grid size factor of 1 and 1.31; see Fig. 5b. The two-dimensional assessment of similar flows and the three-dimension trends provide estimates of the grid-induced error of 10%. The error in mixing efficiency, as shown in Fig. 5c, is greater than the other flowfield properties and the trend is thus a 14% grid-induced overestimation for a grid size factor of 1. The trends with opposed injector array location are expected to remain valid when comparing solutions of similar grid size factors.

Validation

The WARP code has been validated for similar high-speed flows in [10,18,25]. In [18] it has been shown that numerical results obtained by the WARP code were in good agreement with experimental data on the injectant mole fraction distributions, obtained by Donohue et al. [26] for a Mach 2 swept injector, for a relatively low value of the turbulent Schmidt number, $Sc_t = 0.25$. To further substantiate the results of the WARP code validation a wall injection experiment completed at Virginia Tech's blowdown tunnel is recreated. This experiment was previously simulated by Mao et al. [27] using NASA's SPARK code with a Baldwin–Lomax algebraic turbulence model and $Sc_t = 0.5$. Sonic helium with a total pressure of 76 kPa and total temperature of 295 K is injected from an adiabatic wall at a 15 deg angle into a Mach 3 vitiated airstream with a total pressure of 655 kPa and a total temperature of 290 K. A rectangular injectant inflow orifice of area equal to that of the experimental elliptical shape is used in the present simulation to simplify the gridding process. Distances are nondimensionalized by the jet width, $D = 3.175$ mm. A 0.585 m flat plate is simulated upstream of the jet to recreate the experimentally observed $2.2D$ boundary layer height.

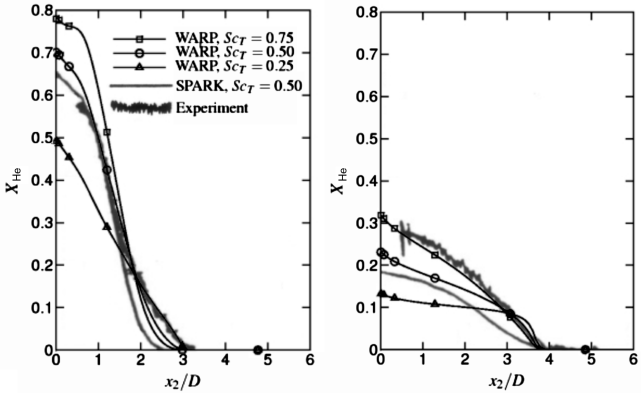

a) $x_1/D = 20$ b) $x_1/D = 90$

Fig. 6 Wall injection of Mao et al. [27]: He mole fractions with x_2/D height above wall downstream of injection jet.

The grid used consisted of $291 \times 126 \times 126 = 4.6$ million nodes. Assuming that Richardson extrapolation of error can be used after the He injection, such that the difference in calculating the solution around the bow shock is minimal, then the grid-induced error in the solution is approximately 2.0%.

For free shear layers the turbulent Prandtl number should be around 0.5, whereas in boundary-layer flow a value of 0.89 or 0.9 is appropriate to obtain the correct temperature profiles and wall heat flux ([22], p. 238). As the jet is low angle, and the experimental results do not show the helium penetration greatly beyond the boundary layer Pr_t is set at 0.9. Calculations are performed with three different turbulent Schmidt numbers, 0.75, 0.5, and 0.25, to assess its influence. Figure 6 illustrates the He mole fraction variation with height above the wall along the jet centerline at two measurement stations. Initially a Sc_t value between 0.25 and 0.5 is needed to provide the levels of mixing observed experimentally. However, by the last measurement station $Sc_t = 0.75$ provides a better estimate of maximum mole fraction and helium spreading. Mao et al. found a 40% underprediction in the maximum He mole fraction at the $90D$ measurement station. WARP overpredicts the maximum mole fraction at the $90D$ station, by approximately 6% for $Sc_t = 0.75$, and underpredicts it by approximately 23 and 57% for $Sc_t = 0.5$ and 0.25, respectively. The results confirm the statement made by Mao et al. that Sc_t should vary in the flowfield to accurately capture the experimental findings.

The use of two different turbulence models, one in [27] and one in the present study, demonstrate the conclusions on the magnitude of Sc_t for hypervelocity turbulent fuel/air mixing processes are independent of the turbulence model used. Finally, the helium mass fraction contours presented in Fig. 7, for the previously considered (see [18]) ramp injection in a Mach 6 air flow by Waitz et al. [28] lends support to the aforementioned validation results. Note that the turbulence Schmidt number has been shown to be low and vary across the mixing layers ([29], p. 49) and that the trend appears in the preceding results. Because of the lack of appropriate experimental results relevant to hypervelocity flow situations, as considered in the present study, the Sc_t and Pr_t numbers are set to generally accepted

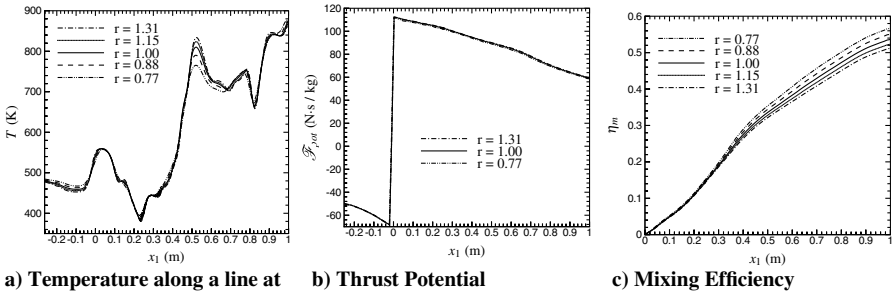

a) Temperature along a line at $x_2 = 0.035$ m, $x_3 = 0.015$ m b) Thrust Potential c) Mixing Efficiency

Fig. 5 Variation in case 3 with grid density.

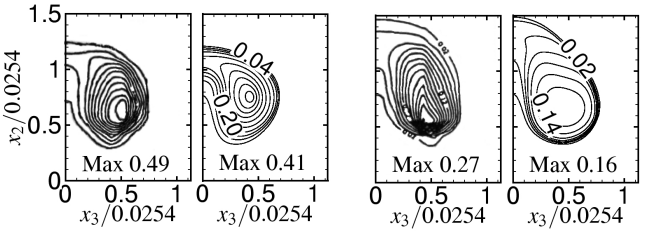

a) x_1 /0.0254 = 8 **b) x_1 /0.0254 = 13**

Fig. 7 Ramp injection of Waitz et al. [28]: helium mass fraction contours. Left: experimental, right: WARP $Sc_t = 0.25$.

values of 1.0 and 0.9, respectively. This offers a conservative estimate of the mixing in this study; however, the trends in mixing will still be valid.

Flow Behavior

The two-dimensional shcramjet inlet for a 0.03 m array separation is shown in Fig. 8. The inlet boundary layer, of height 50–65 mm depending on the case, separates around the corner of the horizontal duct as it interacts with the cowl shock, at $x_1 \approx -0.36$ m. This creates only a small recirculation zone, with a height less than 0.5 mm, and for all cases reattaches within a 0.01 m distance downstream. The length of the inlet before the injectors is 2.13, 1.85, and 1.72 m for array separations of 0.03, 0.02, and 0.01 m, respectively. The cowl starts at $x_1 = -0.955$, -0.872, and -0.789 m for the three array separations with a wall boundary condition along the bottom of the computational domain downstream from this location. The bulk flow before the injectors has properties of approximately a 3316 m/s velocity, a 482 K temperature, a 5007 Pa pressure, and a Mach number of 7.56.

Upon reaching the cantilevered ramp injectors vorticity in the airflow is generated around the cantilevered ramp injectors due to cross-stream shear as the air "spills" from the high-pressure region above the injectors into the low-pressure troughs between them. Two strong counter-rotating vortices are formed behind the bluff body of each injector, and the vorticity is further enhanced by baroclinic effects due to fuel density gradients and the base shock formed at the end of the injector. Figure 9 illustrates the pressure contours in case 2, with the bow shocks forming on top of the injectors, starting at $x_1 = -0.226$ m, and the base shocks forming as the expanded flow returns to parallel the mixing duct walls at $x_1 = 0$ m. The combination of opposing and reflected shocks creates a train of periodic high-pressure regions in the mixing duct. With the injector geometries and separations used in the present study the base and bow shocks are found to combine after the first reflection of the bow shock.

The low-pressure region under the injectors in conjunction with the strong vortices initially draws the fuel towards the walls. The fuel entrained in the vortices subsequently rotates away from the walls. The base shocks serve to further lift the fuel jets away from the walls. Subsequently the shocks from the opposing injector array, both bow and base shocks, interact to force the fuel jets back towards the walls from which the jets originated. Continuing downstream, the fuel jet undulates in the vertical, x_2, dimension as shocks impinging from

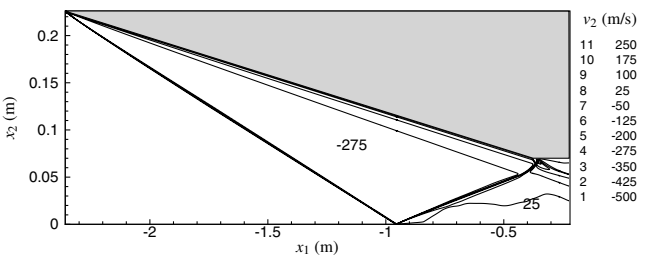

Fig. 8 Inlet shocks observed in v_2 velocity contours (0.03 m array separation).

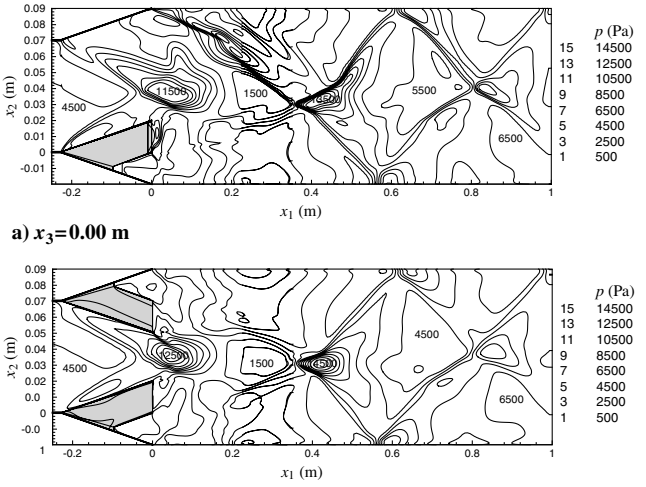

a) x_3=0.00 m

b) x_3=0.01 m

Fig. 9 Case 2: pressure contours.

across the duct turn the flow, reflect from the wall, and turn the flow back in the opposite direction.

Effect of Array Displacement

Shocks from the opposing injector arrays play a major role in the mixing behavior. Strong shocks redirect the flow passing through them in the vertical, x_2, dimension. For array displacements of -0.02 and 0 m the bow shocks created above the injectors combine to form almost a continuous shock front across the computational domain. Figure 10 illustrates the pressure contours at $x_1 = -0.1$ m for cases 2 and 4, with array displacements of 0 and 0.02 m, respectively, in which the shocks are represented by the closely spaced contours. When these shocks interact with the fuel jet originating from the injectors on the opposite walls they redirect the fuel, which initially migrates towards the duct center, back towards the duct walls. For larger array displacements the bow shocks degrade quickly to the sides of the fuel injectors; see Fig. 10b for case 4. This means the shocks that interact with the opposing fuel jets are weaker or nonexistent at the spanwise, x_3, location of the fuel.

The hydrogen mass fraction contours for cases 2 and 3 are shown in Figs. 11 and 12, respectively, for x_1 planes through the length of the mixing duct. Contours for all figures of hydrogen mass fractions extend exponentially from 0.01 to 1.0 with the stoichiometric mass

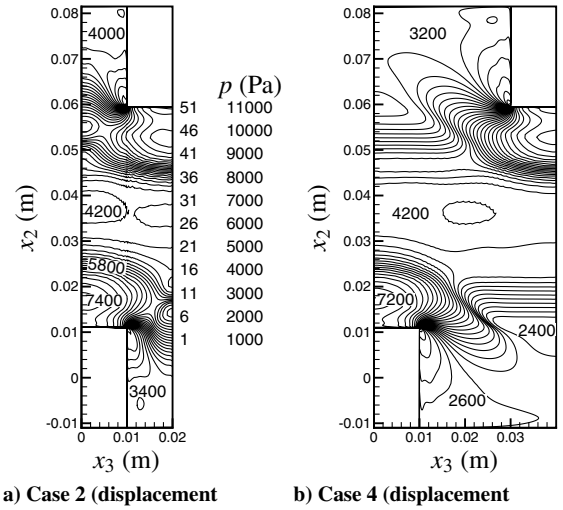

a) Case 2 (displacement = 0.00 m) **b) Case 4 (displacement = 0.02 m)**

Fig. 10 Pressure contours at $x_1 = -0.1$ m (injector structures located at bottom left and top right).

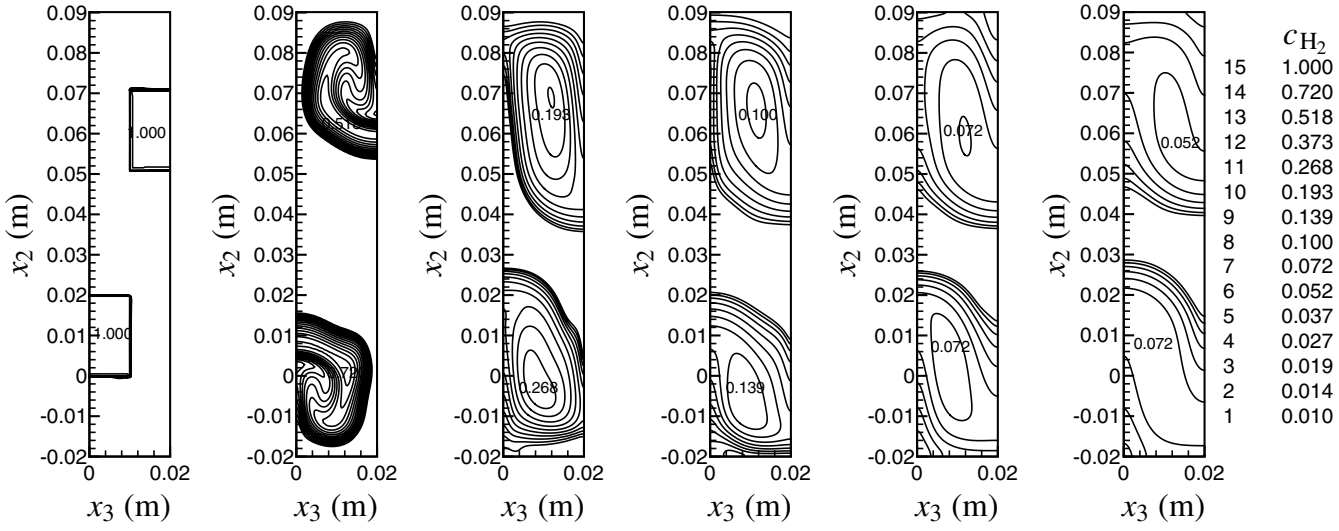

a) $x_1 = 0$ m **b)** $x_1 = 0.2$ m **c)** $x_1 = 0.4$ m **d)** $x_1 = 0.6$ m **e)** $x_1 = 0.8$ m **f)** $x_1 = 1.0$ m

Fig. 11 Hydrogen mass fraction contours for case 2.

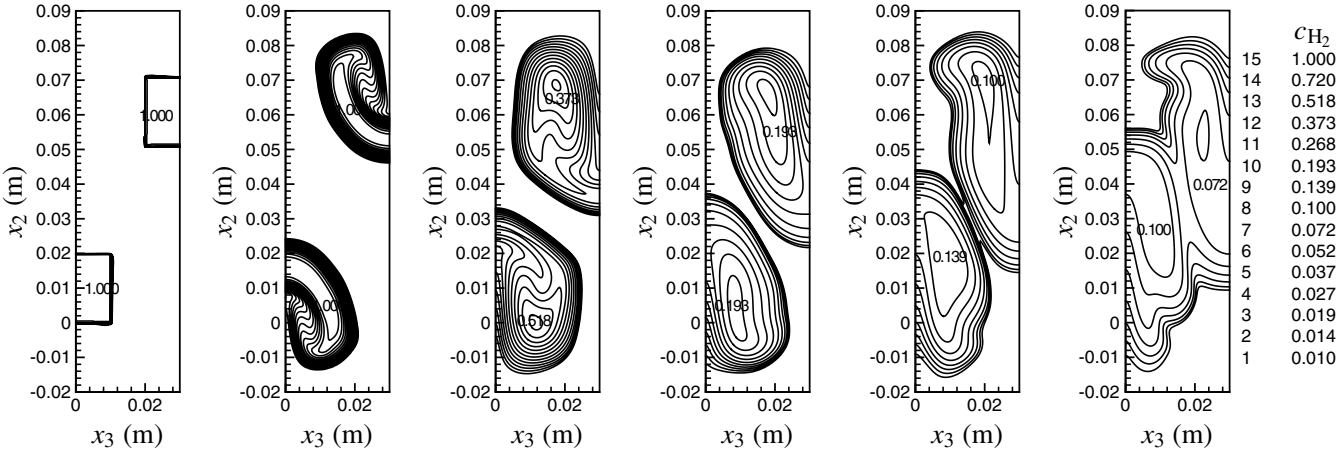

a) $x_1 = 0$ m **b)** $x_1 = 0.2$ m **c)** $x_1 = 0.4$ m **d)** $x_1 = 0.6$ m **e)** $x_1 = 0.8$ m **f)** $x_1 = 1.0$ m

Fig. 12 Hydrogen mass fraction contours for case 3.

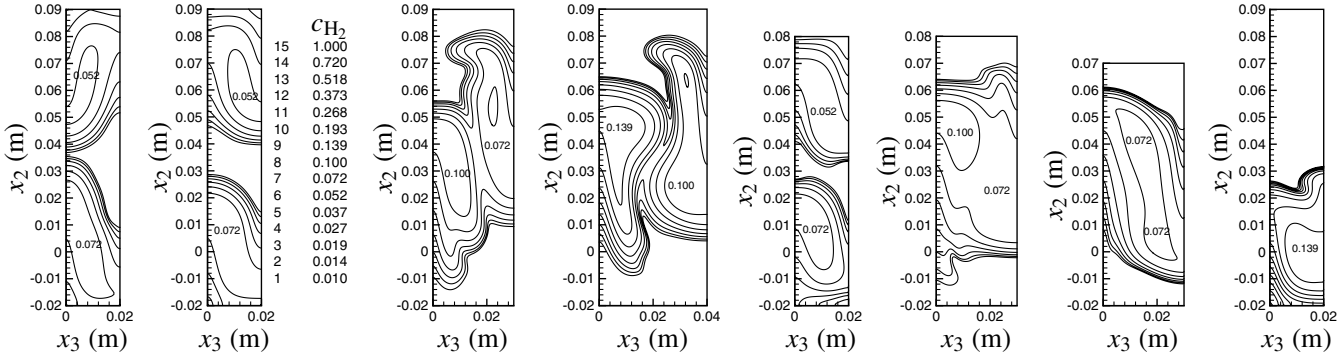

a) Case 1 **b) Case 2** **c) Case 3** **d) Case 4** **e) Case 5** **f) Case 6** **g) Case 7** **h) Case 8**

Fig. 13 Hydrogen mass fraction contours at end of the mixing duct ($x_1 = 1.0$ m).

fraction lying at 0.02876. Only the computational domain is shown for each case, between the symmetry planes through the centers of the cowl and body injectors. For all figures of x_1 cross sections the cowl wall lies at $x_2 = -0.02$ m and the body wall location depends on duct height. Comparing these two cases it can be seen that the maximum H_2 mass fraction is reduced more quickly in case 2. Also clearly evident in the fuel structure in the top and bottom of the duct is the asymmetry of the mixing along the cowl and body. For array displacements of -0.02 and 0.00 m the shocks reflected throughout the mixing duct prevent fuel jet penetration and a core of unmixed air is retained in the center of the duct, as seen in Fig. 11. For array displacements of 0.01 and 0.02 m the weak opposing shocks allow fuel jet penetration and a combination of the fuel from injectors on opposite walls in the center of the duct; see Fig. 12.

For mixing at high convective Mach number, the two main mixing mechanisms are the shear layers and the strong axial vortices generated by cantilevered injectors [12]. The location of the vortices in relation to the fuel/air interfaces thus plays a major role in the mixing achieved. For array displacements of −0.02 and 0 m the vortices remain in the vertical half of the duct in which they originate. For 0.01 and 0.02 m array displacements the vortices migrate to the duct center, in both the vertical dimension and the spanwise computational domain, and coalesce into a single vortex. Similar to studies of single arrays of cantilevered ramp injectors it is found that the larger the array displacement the stronger the axial vortices generated. The stronger vortices entrain more air under the fuel jets and provide a greater buffer between the fuel and the boundary layers on the duct walls. The strong vortices are deteriorated by viscous effects and also by the large number of shocks through which they pass. This degrades their effectiveness at mixing fuel and air when compared with studies for cantilevered injectors over flat plates, which contain no reflected shocks [10].

The hydrogen mass fraction contours at the end of the mixing duct, Fig. 13, exhibit higher peak fuel concentrations as the array displacement is increased in Figs. 13a–13d. Equivalence ratios in all cases are close to those needed for combustion in all fuel regions. The maximum equivalence ratio ranges from 2.3 in case 1 to 5.0 in case 4.

Effect of Array Separation

When the array separation is reduced, the form of the dominant shock structure is not significantly affected. A reduction in array separation reduces the distance to which the fuel must penetrate the airstream allowing for better mixing. For a constant array displacement of 0.01 m, the array separation is reduced from 0.03 to 0.02 to 0.01 m in cases 3, 6, and 7, respectively. Comparing these cases in Fig. 13 illustrates that a reduction in array separation reduces the pure air regions in the flow cross section. This solution to mixing creates greater relative flow blockage from the injectors and increases the frictional losses compared with the overall mass flow. Losses increase as the flow passes through more reflected shocks, compared with greater array separations, over a fixed mixing length. Cases 2 and 5, which have a 0 m displacement, show similar trends with the reduction in array separation.

Global Performance Parameters

One of the commonly used measures of mixing performance is the decay in maximum H_2 mass fraction with downstream distance. The overall mixing to stoichiometric levels is assumed to occur at a similar pace with the decay in the maximum fuel mass fraction. However, to more stringently quantify the mixing enhancement, the air-based mixing efficiency at a streamwise plane of interest is defined as the ratio of the oxygen that would burn in the plane to the mass flux of oxygen entering the engine.

$$\eta_m = \int_b c^R_{O_2}\, \mathrm{d}\dot{m}/(0.234 \times \dot{m}_{\mathrm{air,engine}}) \tag{1}$$

The mass fraction of reacting oxygen, $c^R_{O_2}$, is given as

$$c^R_{O_2} = \min\left(c_{O_2}, c^S_{O_2} \times c_{H_2}/c^S_{H_2}\right) \tag{2}$$

with the stoichiometric mass fraction of oxygen, $c^S_{O_2}$, equal to 0.2284 and the stoichiometric mass fraction of hydrogen, $c^S_{H_2}$, equal to 0.02876. Note that this formulation does not take into account the flammability limits of hydrogen in air, which are $0.1 < \phi < 7.0$ at standard pressure and have been shown to lie above $\phi = 0.8$ for cases similar to the ones studied here [13].

The mass flux averaged stagnation pressure is not appropriate to assess the losses incurred due to the significant total temperature variations in the mixing region. The thrust potential is therefore used, which measures the difference in momentum between a plane of interest and the flow in that plane reversibly expanded to an iteratively determined back pressure at the nozzle exit area of the shcramjet [11]. To minimize the drag losses the nozzle exit area is taken to be the same as the inlet area. Thrust potential is thus defined as

Table 3 Performance parameters at end of mixing duct ($x_1 = 1.0$ m)

Case	Array displacement, m	Array separation, m	M_c	η_m	$\mathcal{F}_{\mathrm{pot}}$, N · s/kg	$\mathcal{F}_{\mathrm{pot}}$ gain, N · s/kg	$\mathcal{F}_{\mathrm{pot}}$ losses, N · s/kg
Variation in array displacement							
1	−0.02	0.03	0.85	0.627	23.7	166.3	−142.6
2	0.00	0.03	0.85	0.598	21.9	164.1	−142.2
3	0.01	0.03	1.20	0.536	53.9	175.9	−122.0
4	0.02	0.03	1.45	0.459	68.9	181.1	−112.2
Variation in array separation							
3	0.01	0.03	1.20	0.536	53.9	175.9	−122.0
6	0.01	0.02	1.10	0.544	23.2	168.4	−154.4
7	0.01	0.01	0.90	0.517	2.0	171.3	−169.3
Additional cases							
5	0.00	0.02	0.70	0.681	−3.3	168.4	−171.7
8	0.00	0.03	0.85	0.277	35.5	149.2	−113.7
			Case 2 with one array of injectors				
9	0.01	0.02	1.10	0.530	39.4	179.4	−140.0
			Case 6: reacting				
10	0.00	0.0146	0.85	0.642	−3.1	161.8	−164.9
			Case 2 with 7 deg injector compression angle				
11	0.02	0.0146	1.43	0.451	57.5	186.9	−129.4
			Case 4 with 7 deg injector compression angle				
12	0.01	0.02	1.20	0.538	28.4	178.5	−150.1
			Case 6 with lower fuel injection pressure				
13	0.00	0.03	−1.00	0.639	-81.3	63.2	−144.5
			Case 2 with negative convective Mach number				
14	0.00	0.03	1.45	0.516	34.0	182.4	−148.4
			0.01 × 0.01 m injector, 0.03 m under injectors				
15	0.00	0.03	1.45	0.552	27.8	180.6	−152.8
			0.01 × 0.01 m injector, 0.02 m under injectors				
16	0.00	0.03	1.45	0.519	32.2	181.2	−149.0
			0.01 × 0.01 m injector, 0.01 m under injectors				
17	0.01	0.03	2.1	0.627	65.8	186.0	−120.2
			0.01 × 0.01 m injector, 0.02 m under injectors				

$$\mathcal{F}_{\text{pot}} = -\mathcal{F}_{\text{pot,ref}} + \int_b \frac{\rho_c q_c^2 + p_c^\star}{\rho_c q_c} \, \mathrm{d}\dot{m}/\dot{m}_{\text{air,engine}} \tag{3}$$

The reference thrust potential is the thrust potential at the start of the shcramjet, equal to 3411 N · s/kg. The local mass flow rate is determined numerically at each plane b. This insures the mass flow rate corresponds to the sum of the air mass flow and the fuel mass flow, with the fuel mass flow being zero before injection. Friction, mixing, and shock losses act to reduce the thrust potential.

The values of the performance parameters at the end of the mixing duct are summarized for all cases in Table 3. Figure 14a illustrates the mixing efficiency for cases 1 through 4 as the array displacement is increased at a constant 0.03 m array separation. The mixing efficiency is higher for small array displacements. The mixing efficiency initially has a steep rise that is reduced with downstream distance. A bend can be seen in the mixing efficiency for cases 1 and 2 at $x_1 \approx 0.35$ m. This is the location where the fuel jets have expanded to cover the computational span, so the fuel/air contact surface is decreased and diffusive mixing is reduced. Another decrease in mixing efficiency growth occurs at $x_1 \approx 0.6$ m, where the fuel has expanded to the duct walls; thus the only pure air region left to mix with is at the center of the duct. The cases with higher array displacement do not have such dramatic bends due to the fact that there is no drastic reduction of the fuel/air interface. The trends in mixing efficiency are not an artifact of the differing convective Mach number. Previous studies have shown increasing the convective Mach number increases mixing efficiency [10]. As the array displacement is increased so is the convective Mach number, given in Table 3. The mixing efficiency is found to be greater for the smaller array displacement and smaller M_c.

The thrust potential with a constant 0.03 m array separation and increasing array displacement for cases 1 through 4 is presented in Fig. 14b. The initial value of −50 N · s/kg is due to the losses in the shcramjet inlet before the injector arrays. The thrust addition from the fuel momentum, at $x_1 = 0$ m, is greater than all losses incurred in the shcramjet inlet. Thrust potentials exhibit similar trends in all cases; the thrust potential losses are greater for smaller array displacements due to mass flow averaging of stronger shocks across the engine span.

The trends in mixing efficiency and thrust potential with array separation are shown in Fig. 15. Array displacement is constant at 0.01 m and array separation is reduced 0.01 m between successive cases from 3 to 6 to 7. Mixing efficiency is found to increase as the array separation is decreased and the fuel requires less travel to obtain a uniform mixture. A maximum mixing efficiency will be reached with array separation reduction as the flow behavior dictates a relatively smaller fuel/air interface length at smaller array separations. Case 7 with a 0.01 m array separation generates a 0.517 mixing efficiency, reduced from the 0.544 mixing efficiency of case 6 that has a 0.02 m array separation. Case 7 contains a bend in the mixing efficiency due not to fuel reaching the walls, but from the opposing fuel jets combining in the duct center along a fair portion of the fuel/air interface at $x_1 \approx 0.4$ m. Similar trends are observed with the reduction in array separation, in cases 2 and 5 that have a 0 m displacement. Case 5 results in the highest mixing efficiency of the present study, of 0.681.

Of note is the comparative mixing performance of a single array of injectors on the lower wall of the duct, case 8. In this case the lack of

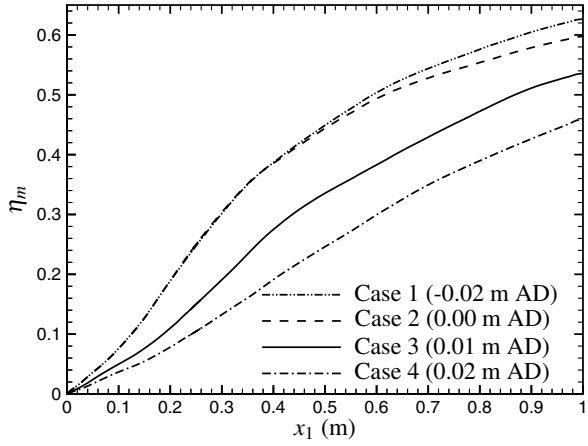

a) Mixing Efficiency

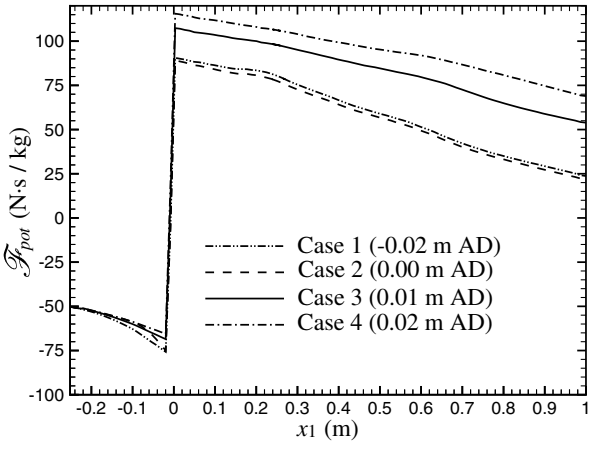

b) Thrust Potential

Fig. 14 Performance parameters for changes in array displacement (AD), for cases 1–4.

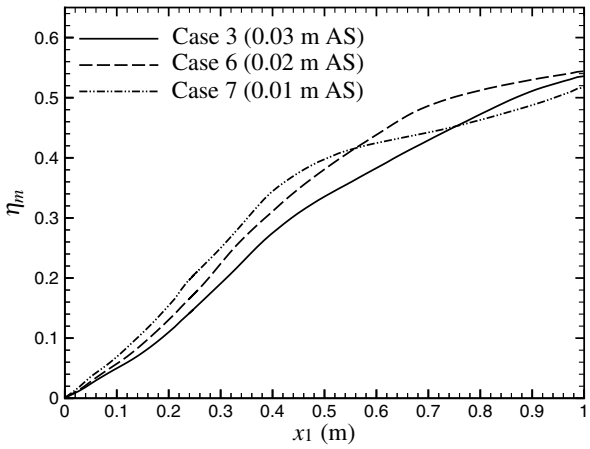

a) Mixing Efficiency

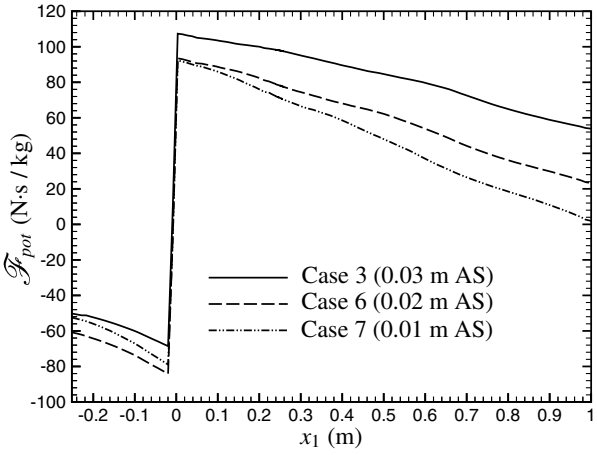

b) Thrust Potential

Fig. 15 Performance parameters for changes in array separation (AS) for cases 3, 6, and 7.

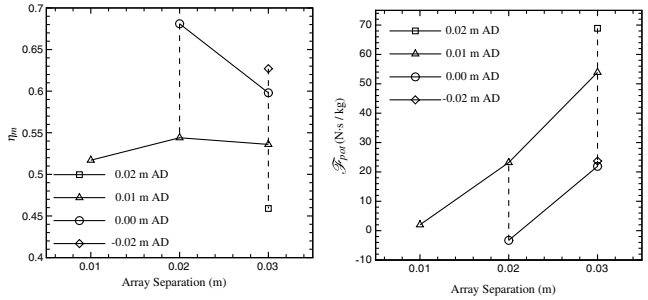

a) Mixing Efficiency **b) Thrust Potential**

Fig. 16 Performance parameter variation at end of mixing duct for cases 1–7 (AD denotes array displacement).

opposing shocks results in fuel jet penetration that is initially superior to that of case 2. However, the bow and base shock reflections compress the fuel jet to only 47% of the vertical duct height by the end of the mixing duct; see Fig. 13h. Opposed injectors produce greater amounts of air under the fuel jets when compared with a single array with the same inflow conditions, which would require the injectors in a single array to lie closer together. The single array of injectors on the lower wall exhibited the greatest equivalence ratios at the end of the mixing duct with a maximum of approximately 6.7. The mixing efficiency is at all streamwise planes less than half of that found in case 2, with a 0.277 mixing efficiency at the end of the mixing duct. This is attributed mostly to the 50% reduction in initial fuel/air interface area that limits the shear mixing created. In contrast, case 4, with the same ratio of initial fuel injection area to air area, provides a 66% greater mixing efficiency.

The trends in mixing efficiency and thrust potential with relative injector locations are summarized in Fig. 16.

Premature Ignition

The preferred mixing flow configuration in the present study is the configuration that does not ignite prematurely ahead of the combustion-inducing shock. The compression process from shocks originating from both the body and cowl allows for configurations in which the fuel jets migrate away from the hot wall surfaces and occupy a significant vertical portion of the duct. Case 6 provides the greatest mixing efficiency, 0.544, for a case in the parametric study that is likely to avoid premature ignition. In this case, by $x_1 = 1.0$ m, the flow has approximately a uniform fuel mass fraction except for a good air buffer between the combustible fuel mixture and the boundary layers, Fig. 13f.

A chemically reacting case using a nonequilibrium chemical reaction model confirms the validity of the nonreacting studies performed. The chemical source term is calculated using a 20-reaction, 9-species nonequilibrium chemical model modified from that of Jackimoski [14]. Reactions of nitrogen are ignored as they have been shown to be negligible in similar cases [1]. All other parameters are the same as those used in the nonreacting cases. A comparison to the cases conducted by Schwartzentruber et al. [13] for similar shcramjet conditions suggest that the grid density should be sufficient to capture the onset of premature ignition.

To confirm the absence of premature ignition, case 6 is repeated (case 9). The only difference in chemical composition is minute amounts, mass fractions on the order of 10^{-5}, of molecular oxygen dissociated in the boundary layers. No regions containing a flammable fuel mixture attain temperatures great enough for combustion. Slight variations exist between the reacting and nonreacting cases with 2% less mixing efficiency found in the reacting case by the end of the mixing duct.

Injector Array Modifications

In an effort to further quantify mixing effects and to enhance the positive aspects of fuel/air mixing via fuel injection from arrays on opposing walls, a number of modifications are performed.

Increased Injector Compression Angle (Cases 10 and 11)

As cases with smaller array displacements give superior mixing efficiencies, but are likely to prematurely ignite, the compression angle of the injectors in case 10 is increased from 5 to 7 deg, while maintaining all other parameters as in case 2. The fuel injection planes are thus closer to the center of the duct and the fuel has a greater velocity component towards the center of the duct. This configuration increases mixing efficiency by 7% over case 2 with the stronger bow shocks generating 16% greater thrust potential losses. The detrimental thrust losses associated with increasing injector angle become more pronounced in the mixed-compression as opposed to the external-compression shcramjet due to the reflection of the stronger shocks. The initial fuel placement and velocity is insufficient to overcome the increased strength of the spanwise continuous bow shock and a flowfield very similar to case 2 results with the fuel mixture entering the boundary layer.

Case 11, which has a similar 7 deg injector compression angle and the wider array displacement used in case 4, provides a small decrease in mixing efficiency and a 15% increase in thrust potential losses over case 4 by the end of the mixing duct. The increased angle does initially improve mixing efficiency, with a 20% greater mixing efficiency than case 4 at $x_1 = 0.6$ m. The stronger vortices found in the flow act to reduce the fuel/air interface in the latter regions of the mixing duct, resulting in a reduced mixing efficiency growth rate.

Reduced Fuel Injection Pressure (Case 12)

The fuel inflow requirements used result in relatively high fuel injection temperatures in some cases, such as 530 K for case 6. The temperature of the fuel must be low enough to cool the boundary layer formed on the cantilevered injector and prevent premature ignition at the point of fuel injection. It is therefore important to have cool fuel, which is also closer to the static temperatures hydrogen would be expected to achieve after being used to cool the airframe of a hypersonic vehicle. The fuel pressure is reduced from 5007 to 3000 Pa, which is still within the 1000–8500 Pa air pressure range beside the fuel injectors. The fuel injection temperature thus drops to 335 K, whereas the mean flow temperature by the end of the mixing duct is reduced from 850 to 750 K. The mixing behavior is minimally affected from that of case 6 with only a 1% drop in mixing efficiency and under a 3% increase in thrust potential. This difference is theorized to be due to the reduced fuel jet expansion into the air flow. This case shows the importance of the fuel injection conditions. The overall mixing behavior is unaffected; however, the flow temperatures can be quite important to initiation of shock-induced combustion in the combustor.

Negative Convective Mach Number (Case 13)

Prior studies [10] have shown a negative convective Mach number, in which the fuel velocity is less than that of the air, can provide similar or superior mixing efficiencies to a positive M_c. Case 2 is repeated with $M_c = -1$, resulting in a reduced fuel velocity and temperature. Mixing efficiency is increased 6.9% to 0.639, from 0.598 in case 2. The thrust potential losses are only 1.6% greater at -144.5 N · s/kg, with the slower fuel reducing the thrust potential gain from 164.1 to 63.2 N · s/kg. A tradeoff thus exists as the increase in mixing most likely will not outweigh the fuel thrust loss, but injection at lower speeds is more practical to obtain.

Injector Size and Expansion (Cases 14–17)

Injectors with a 0.01×0.01 m fuel injection area are explored. An array displacement of 0 m and an array separation of 0.03 m results in a 0.03 m distance to the wall under the fuel injection plane, case 14 in Fig. 17. The small spanwise distance in the 0.01 m wide computational domain dictates little variation in flow properties across the computational span after $x_1 \approx 0.6$ m. Similar spanwise uniformity was not observed in case 2 until $x_1 \approx 1.0$ m. Mixing efficiency, shown in Fig. 18, is initially greater than all previous cases due to the high convective Mach number used, $M_c = 1.45$ as opposed to $M_c = 0.85$ in case 2. Flow conditions dictate a high fuel

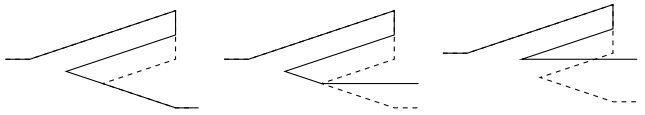

Fig. 17 Flow expansion beneath 0.01 × 0.01 m cantilevered injectors (case 2 for 0.02 × 0.02 m injectors shown in dashed lines).

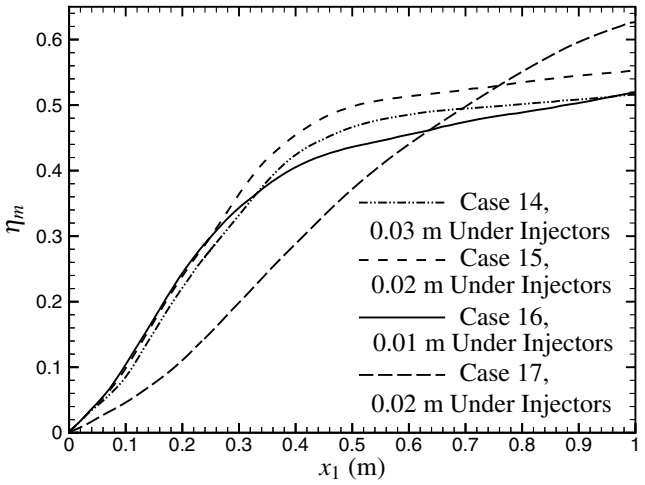

Fig. 18 Mixing efficiency for cases 14–17.

density and a greater mass flow in the shear layers resulting in increased mixing. Mixing efficiency declines as fuel reaches the walls near $x_1 \approx 0.38$ m, indicating premature ignition might occur.

The effect of decreasing the expansion region under the cantilevered injector is coupled to increased shock reflections in the resulting smaller duct height. The distance between the fuel injection planes and the duct walls is reduced from 0.03 m in case 14 to 0.02 m in case 15 and 0.01 m in case 16, Fig. 17. Mixing efficiency rates, Fig. 18, are found to decrease as the fuel reaches the duct walls. This occurs sooner with less expansion under the injector: at $x_1 \approx 0.38$ m, $x_1 \approx 0.32$ m, and $x_1 \approx 0.22$ m for the three cases. At this point mixing efficiencies increase at a much slower rate with mixing due primarily to the shear-layer mixing at the duct center. Mixing duct length for these injectors could be reduced by half, to 0.5 m, with a loss of between only 9 and 17% in mixing efficiency, and a reduction in thrust potential loss of over 20%.

Case 17 has an array displacement of 0.01 m and a 0.02 m distance between the fuel injection planes and the duct walls; see Fig. 17. Mixing characteristics are similar to those of case 3 with fuel in the center of the duct. The mixing efficiency, Fig. 18, does not experience the dramatic decrease in growth, as observed to occur in cases 14 through 16, because the fuel never contacts the duct walls. A 17% increase in mixing efficiency over case 3 is attributed to the considerably greater convective Mach number of the fuel injection and to a lesser extent the reduced duct height and shocks that are weaker on a mass flow averaged basis. The 0.627 mixing efficiency is the greatest of the cases that are expected to avoid premature ignition. The smaller fuel injection areas can provide similar mixing efficiency and thrust potentials as larger 0.02×0.02 m fuel injection areas with no changes in the main mixing mechanisms observed other than the reduced strength of the strong vortices created under the injectors.

Conclusions

A parametric study of the relative locations of fuel injector arrays located on opposing walls was conducted for three-dimensional, turbulent mixing in the inlet of a mixed-compression shcramjet engine. For small array displacements shocks from opposing injector arrays limit jet liftoff and the fuel jets and vortices remain in the vertical half of the inlet duct from which they originated. As the array displacement is increased, weakened opposing shocks allow migration and combination of the fuel jets and vortices into the center of the duct with an air buffer along the walls preventing fuel contact with the boundary layer. Flow behavior that decreases the length of the fuel/air interface, either the fuel jet contacting the wall or the pairing of vortices, decreases the mixing efficiency growth. The mixing efficiency is greatest for array displacements equal to the injector width. Array separation adjustment produces a maximum at a 0.02 m.

Mixing efficiencies for opposed wall injector arrays in a mixed-compression shcramjet range from 0.459 to 0.681. Further increases in mixing efficiency are possible with a thorough study into optimizing the individual fuel injector geometries; increasing the injector compression angle 2 deg resulted in a 0.044 increase in mixing efficiency herein. The use of fuel injection from two walls provides an inherent advantage in mixing over a single wall, as in an external-compression shcramjet. Maximum mixing efficiencies are shown to be 42% greater than the maximum found in the external-compression shcramjet inlet of [7]. The very high-speed fuel injection adds a considerable gain in thrust potential and in most cases outweighs the loss.

To ensure no premature ignition in shcramjet applications, no fuel must enter the hot hypersonic boundary layer. Fuel is found to enter the boundary layer for small array displacement distances due to two effects. Primarily, shocks originating from the opposing injectors redirect the fuel flow away from the duct center and towards the boundary layers. Secondly, the air cushion under the fuel is reduced via weaker axial vortices and a low mass flux of air flowing under the fuel at the point of injection.

The length of the mixing duct must be chosen to be commiserate with the growth in mixing efficiency and fuel placement. By the end of the inlet an array displacement of 0.01 m provided a near uniform fuel mixture in the center of the inlet duct, with an air buffer between the fuel and hot boundary layers. Further assessment of the best mixing configuration will depend to a certain extent on the configuration of the combustion generating shocks and assessment of the combustor performance.

Acknowledgment

This work has been supported by the Natural Sciences and Engineering Research Council (NSERC).

References

[1] Dudebout, R., Sislian, J. P., and Oppitz, R., "Numerical Simulation of Hypersonic Shock-Induced Combustion Ramjets," *Journal of Propulsion and Power*, Vol. 14, No. 6, 1998, pp. 869–879.

[2] Sislian, J. P., Dudebout, R., Schumacher, J., Islam, M., and Redford, T., "Incomplete Mixing and Off-Design Effects on Shock-Induced Combustion Ramjet Performance," *Journal of Propulsion and Power*, Vol. 16, No. 1, 2000, pp. 41–48.

[3] Vasilev, V. I., Zakotenko, S. N., Krasheninnikov, S. J., and Stepanov, V. A., "Numerical Investigation of Mixing Augmentation Behind Oblique Shock Waves," *AIAA Journal*, Vol. 32, No. 2, 1994, pp. 311–316.

[4] Livingston, T., Segal, C., Schindler, M., and Vinogradov, V. A., "Penetration and Spreading of Liquid Jets in an External-Internal Compression Inlet," *AIAA Journal*, Vol. 38, No. 6, 2000, pp. 989–994.

[5] Owens, M., Mullagiri, S., Segal, C., and Vinogradov, V. A., "Effects of Fuel Preinjection on Mixing in Mach 1.6 Airflow," *Journal of Propulsion and Power*, Vol. 17, No. 3, 2001, pp. 605–610.

[6] Guoskov, O. V., Kopchenov, V. I., Lomkov, K. E., and Vinogradov, V. A., "Numerical Research of Gaseous Fuel Preinjection in Hypersonic Three-Dimensional Inlet," *Journal of Propulsion and Power*, Vol. 17, No. 6, 2001, pp. 1162–1169.

[7] Sislian, J. P., and Parent, B., "Hypervelocity Fuel/Air Mixing in a Shcramjet Inlet," *Journal of Propulsion and Power*, Vol. 20, No. 2, 2004, pp. 263–272.

[8] Wilcox, D. C., "Reassessment of the Scale Determining Equation for Advanced Turbulence Models," *AIAA Journal*, Vol. 26, No. 11, 1988, pp. 1299–1310.

[9] Sislian, J. P., and Schumacher, J., "A Comparative Study of Hypervelocity Fuel/Air Mixing Enhancement by Ramp and Cantilevered Ramp Injectors," AIAA Paper 99-4873, Nov. 1999.

[10] Parent, B., Sislian, J. P., and Schumacher, J., "Numerical Investigation of the Turbulent Mixing Performance of a Cantilevered Ramp Injector," *AIAA Journal*, Vol. 40, No. 8, 2002, pp. 1559–1566.
[11] Parent, B., and Sislian, J. P., "Effect of Geometrical Parameters on the Mixing Performance of Cantilevered Ramp Injectors," *AIAA Journal*, Vol. 41, No. 3, 2003, pp. 448–456.
[12] Parent, B., and Sislian, J. P., "Impact of Axial Vortices on Mixing at a High Convective Mach Number," *AIAA Journal*, Vol. 41, No. 7, 2003, pp. 1386–1388.
[13] Schwartzentruber, T. E., Sislian, J. P., and Parent, B., "Suppression of Premature Ignition in the Premixed Inlet Flow of a Shcramjet," *Journal of Propulsion and Power*, Vol. 21, No. 1, 2005, pp. 87–94.
[14] Jackimoski, C. J., "An Analytical Study of Hydrogen-Air Reaction Mechanism with Application to Scramjet Combustion," NASA TP 2791, 1988.
[15] Schumacher, J., "Numerical Simulation of Cantilevered Ramp Injector Fields for Hypervelocity Fuel/Air Mixing Enhancement," Ph.D. Thesis, Graduate Dept. of Aerospace Science and Engineering, Univ. of Toronto, Toronto, 2000.
[16] *The U.S. Standard Atmosphere (1976)*, U.S. Government Printing Office, Washington, D.C., 1976.
[17] Parent, B., and Sislian, J. P., "The Use of Domain Decomposition in Accelerating the Convergence of Quasihyperbolic Systems," *Journal of Computational Physics*, Vol. 179, No. 1, 2002, pp. 140–169.
[18] Parent, B., and Sislian, J. P., "Validation of Wilcox k–ω Model for Flows Characteristic to Hypersonic Airbreathing Propulsion," *AIAA Journal*, Vol. 42, No. 2, 2004, pp. 261–270.
[19] Wilcox, D. C., "Dilatation-Dissipation Corrections for Advanced Turbulence Models," *AIAA Journal*, Vol. 30, No. 11, 1992, pp. 2639–2646.
[20] McBride, B. J., and Reno, M. A., "Coefficients for Calculating Thermodynamic and Transport Properties of Individual Species," NASA TM 4513, 1993.
[21] Yee, H. C., Klopfer, G. H., and Montagné, J. L., "High-Resolution Shock-Capturing Schemes for Inviscid and Viscous Hypersonic Flows," *Journal of Computational Physics*, Vol. 88, No. 1, 1990, pp. 31–61.
[22] Wilcox, D. C., *Turbulence Modeling for CFD*, 2nd ed., DCW Industries, La Cañada, CA, 1998.
[23] Oberkampf, W. L., and Blotter, F. G., "Issues in Computational Fluid Dynamics Code Verification and Validation," *AIAA Journal*, Vol. 36, No. 5, 1998, pp. 687–695.
[24] Roache, P. J., "Verification of Codes and Calculations," *AIAA Journal*, Vol. 36, No. 5, 1998, pp. 696–702.
[25] Fusina, G., Sislian, J. P., and Parent, B., "Formation and Stability of Near Chapman-Jouguet Standing Oblique Detonation Waves," *AIAA Journal*, Vol. 43, No. 7, 2005, pp. 1591–1604.
[26] Donohue, J. M., McDaniel, J. C., and Haj-Hariri, H., "Experimental and Numerical Study of Swept Ramp Injection into a Supersonic Flowfield," *AIAA Journal*, Vol. 32, No. 9, 1994, pp. 1860–1867.
[27] Mao, M., Riggins, D. W., and McClinton, C. R., "Numerical Simulation of Transverse Fuel Injection," NASA, Lewis Research Center N91-21062 13-02, 1991.
[28] Waitz, I. A., Marble, F. E., and Zukoski, E. E., "Investigation of a Contoured Wall Injector for Hypervelocity Mixing Augmentation," *AIAA Journal*, Vol. 31, No. 6, 1993, pp. 1014–1021.
[29] Launder, B. E., and Spalding, D. B., *Lectures in Mathematical Models of Turbulence*, Academic Press, London, 1972.

G. Candler
Associate Editor